ChemPubSoc Europe

DOI: 10.1002/ejic.201800935

EurJIC European Journal of Inorganic Chemistry

Full Paper

Non-Innocent Ligands

Probing Redox Noninnocence of Copper and Zinc Bis-pyridylpyrrolides

Jaime A. Flores,[a] José G. Andino,[a] Richard L. Lord,[b] Robert J. Wolfe,[a] Hyunsoo Park,[a] Maren Pink,[a] Joshua Telser,*[c] and Kenneth G. Caulton*[a]

Abstract: A series of complexes of divalent copper and zinc carrying two systematically substituted 2,2′-pyridylpyrrolide ligands, designated L^n to indicate the number of pyrrole CF_3 substituents (n = 0, 1, 2), have been studied for their geometric and electronic structures. These reveal the pyridylpyrrolide to be a highly anisotropic nitrogen donor ligand which distorts ML_2 complexes away from both planar and tetrahedral structures. Characterization includes CV and mass spectrometry, which show access to cations beyond conventional maximum metal oxidation states. EPR studies at multiple microwave frequencies of the series $Cu(L^n)_2$ gave insight into the substituent effect on frontier orbital composition of these complexes. While $Cu(L^2)_2$ exhibited EPR spectra that were roughly comparable to those for typical, tetragonally distorted Cu^{II} complexes with the SOMO having $d_{x^2-y^2}$ character, the other two complexes exhibited more unusual EPR spectra indicative of their distinct geometry, reminiscent of equatorially-vacant trigonal bipyramidal hybridization and fully consistent with the X-ray crystal structure determinations of all three $Cu(L^n)_2$. DFT calculations map both geometric and delocalization changes upon redox change, and show the relevance of oxidation at the pyrrolide donors rather than at the metal.

Introduction

We have the goal of synthesis of terminal oxido, imino, or even halido complexes on formally highly oxidized late transition metal ML_n complexes. In order to share the burden of oxidation being only at the metal, redox active ligands are attractive ancillaries in targeted L_2MO, $L_2M(NR)$, or L_2MCl_n complexes. A variety of ligands has been historically chosen for this purpose, as shown in Scheme 1, which depicts the ligand redox cycling. For E = O in Scheme 1, this cycling involves quinone, semiquinone, and catecholate forms.

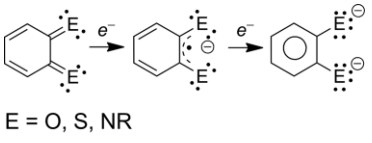

Scheme 1.

This cycling generally involves *reduction* of oxidized ligand forms. We seek ligands whose conventional oxidation level is low, and thus *oxidation* facilitates reactivity enhancement. For example, the ionization potential of pyrrole is 1.0 eV less than that of benzene or pyridine.[1] Thus we expect that the filled π orbitals of a pyrrole may, in its metal complexes, share the oxidation(s) that classically occur at the metal alone. Hammett studies have shown[2] that pyrroles are π-donors when attached to phenyl via either N or any pyrrole ring carbon. As a substituent on an aryl (or pyridine) ring, a pyrrolide is a donor not only to metal,[3] but it also gives amide character to the pyridine partner, provided there is conjugation between the two rings (Scheme 2).

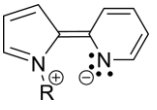

Scheme 2.

Collective oxidation should be easier if the ligand is delocalized, so an *ortho*-attached pyridyl on the pyrrolide is desirable. For oxidative applications, it is especially appropriate to have both N donors at the imine oxidation level, since, unlike amines, these cannot be dehydrogenated (i.e., easily oxidized), and certainly the imine nitrogen lone pair itself resists further oxidation.

The combination of *two* pyridylpyrrolides assembles two imines and two pyrrolides, which is the same donor set found in porphyrins, as noted by Betley and co-workers,[3g,3m] but with the difference that the two bidentate ligands have more flexibility than the porphyrin macrocycle. We thus have stereoelectronic flexibility not found for porphyrins, but retain much of their redox capacity.

[a] *Department of Chemistry, Indiana University, 800 East Kirkwood Avenue, Bloomington, Indiana 47405 USA*
E-mail: caulton@indiana.edu
https://www.indiana.edu/~kgcgroup/
[b] *Department of Chemistry, Grand Valley State University, Allendale, Michigan 49401 USA*
[c] *Department of Biological, Physical and Health Sciences, Roosevelt University, 430 South Michigan Avenue, Chicago, Illinois 60605 USA*
E-mail: jtelser@roosevelt.edu
https://blogs.roosevelt.edu/jtelser/

Supporting information and ORCID(s) from the author(s) for this article are available on the WWW under https://doi.org/10.1002/ejic.201800935.

The report by the McNeill group[4] of a convenient synthesis of pyridyl pyrrolides thus drew us to explore mid (Fe) to late (Ni) transition metal complexes of that ligand class (Scheme 3, bottom).[5]

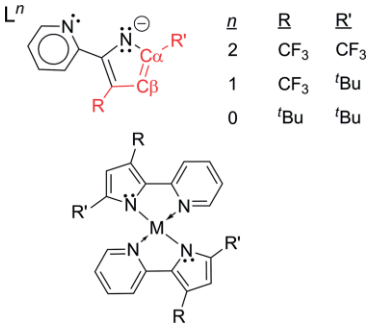

Scheme 3.

In the McNeill synthesis, three pyrrole ligand ring carbons (C2,3,4; shown in red in Scheme 3) derive from a β-diketonate reagent via ring closure of a β-diketone with an aminomethylpyridine. The variety of β-diketones means that a correspondingly wide variety of 3,5-disubstituted pyridylpyrrolides can be prepared. Evaluation of both steric and electronic substituent effects thus becomes possible.[6] While pyrroles are well known to be oxidizable,[7] subsequent coupling of the radical cations to form oligo- and polypyrroles is expected to be less likely if the radical cation is bound to a metal center. The substituent pattern on our pyrrole rings also discourages oxidative coupling/polymerization at the ring carbons: three of the pyrrole ring carbons in HL^n are protected by substitution, and the fourth (at Cβ) is sterically protected.[8,9]

A four-coordinate Ni^{II} complex with a single pyridyl pyrrolide ligand and other ligands {[(py-^{Me}pyrr)Ni(CH_3)(lut)] and [(py-^{Me}pyrr)Ni(Ph)(lut)], lut = 2,4-lutidine} has recently shown interesting reactivity.[10] Other transition metal complexes, with a variety of synthetic, catalytic, and energy transfer applications, which contain a single pyridyl pyrrolide ligand have been reported. Examples include metals such as Pd^{II},[11] Pt^{II},[6a,6c,12] Cu^{I},[13] and Au^{III}.[14] Pincer type complexes have also been reported that contain pyrrolide-pyridine-pyrrolide[15] or pyridine-pyrrolide-pyridine[16] donors with one or more ancillary ligands. Our focus, however, is on the case where we install *two* identical pyridyl pyrrolides on a single metal,[5c,5d] as it is possible that such a ligand pair can be *collectively* redox active, hence subject to either electron loss or gain, when the overall metal complex undergoes redox change. For example, could ZnL_2 be oxidized (electron loss delocalized over the *pair* of appended ligands?), and at lower energy cost than if it were at only one L? Indeed, in one ZnL_2 case already reported,[4b] chemical ionization mass spectrometry (CIMS) detected the cation $[ZnL_2]^+$. All of the above can be modulated by substituents on the pyrrole ring, and so here we investigate both electron withdrawing CF_3 substituents, and electron donating *t*Bu substituents (see Scheme 3). The *t*Bu vs. CF_3 pyrrole substituents are shown here to have a significant impact on both geometric structure and thus d orbital mixing. We are also interested in evaluating the expectation that a CF_3 substituent on C_α of the pyrrole can resist intramolecular attack by a highly electrophilic metal center so that the electrophilicity is focused on bimolecular reactivity. For comparison, it is known that a *t*Bu substituent at C_α can suffer such attack.[6b]

The fact that one pyrrole nitrogen lone pair is to some extent "committed" to the aromaticity of pyrrole is modulated by the fact that the resonance energy of pyrrole is less than that of benzene by ca. 30 % or 10–15 kcal/mol.[17] We address here the determination of the stereo- and electronic characteristics of this ligand class on d^9 Cu^{II}, as well as d^{10} Zn^{II}, as a preliminary to rationally exploring its utility for high oxidation state reactivity studies.

Results and Discussion

Synthesis and Characterization of $Cu(L^n)_2$

Ligand L^2

Reaction of $Cu(OTf)_2$ with KL^2 forms $Cu(L^2)_2$ (Scheme 3: M = Cu, R = R′ = CF_3), identifiable by its dark blue color and its ^{1}H NMR spectrum, with chemical shifts characteristic of a paramagnetic molecule. The magnetic moment at 25 °C was measured as 2.12 Bohr magnetons (Evans method in benzene), corresponding to one unpaired electron, hence Cu^{II} and two monoanionic ligands. A single crystal structure determination (Figure 1) of material crystallized from Et_2O shows it to have crystallographic C_2 symmetry with an N(py)–Cu–N(py) angle of 143.14(12)° and N(pyrr)–Cu–N(pyrr) angle of 154.61(13)°. The Cu–N distance to pyridine is slightly (0.06 Å) longer than to the pyrrolide N. The pyridyl nitrogen lone pairs are directed towards the copper [C(*para*)–N–Cu = 171.4°] while the pyrrolide lone pair misalignment is greater (unequal angles Cu–N–Cα = 113.99° and 138.71°). The two ring planes within a given chelate are nearly coplanar, but the angle between the two MNN planes is 58.4°, thus far from the orthogonal found in a tetrahedron. The coordination geometry is neither planar nor tetrahedral. The structure is thus quite distinct from that of zinc analogs.[4b]

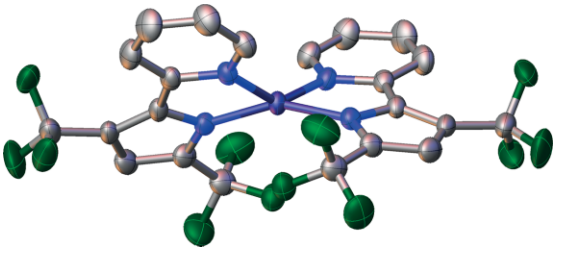

Figure 1. X-ray crystal structure of crystallographically C_2 symmetric $Cu(L^2)_2$. Thermal ellipsoids shown at 50 % probability, hydrogen atoms omitted for clarity. Gray, blue, purple, and green ellipsoids represent C, N, Cu, and F atoms, respectively. Selected structural parameters [Å (°)]: Cu–N(pyrr), 1.9389(19), Cu–N(py), 2.004(2); N(pyrr)–Cu–N(pyrr)′, 154.61(13); N(pyrr)–Cu1–N(py)′, 105.58(8); N(pyrr)–Cu–N(py), 82.55(8); N(py)–Cu1–N(py)′, 143.14(12).

Ligands L^1 and L^0

Reaction of $Cu(OTf)_2$ with KL^1 or KL^0 forms the corresponding $Cu(L^n)_2$. However, we find that a superior approach is to deprotonate HL^1 with TlOEt in Et_2O, and the resulting TlL^1 then reacts

cleanly with $Cu(OTf)_2$ in Et_2O to furnish $Cu(L^1)_2$, whose NMR spectra show one ^{19}F signal, but at least three ^1H NMR signals, one of which has larger intensity, consistent with a *t*Bu group; the "missing" resonances have been sought in the range +400 to –200 ppm, but are apparently too broad to detect. The magnetic moments in benzene at 25 °C were measured (Evans method) as 2.01 and 1.81 Bohr magnetons, respectively for $Cu(L^0)_2$ and $Cu(L^1)_2$, corresponding to one unpaired electron as above with $Cu(L^2)_2$.

The impact of chelate substituents is evident from a structure determination of $Cu(L^1)_2$ (Figure 2) with crystals grown from benzene/pentane.

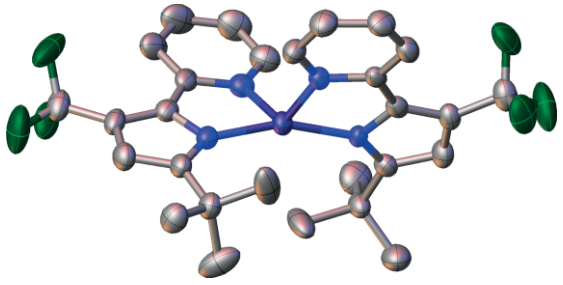

Figure 2. X-ray structure of $Cu(L^1)_2$, showing nitrogen atom labeling. Thermal ellipsoids shown at 50 % probability, hydrogen atoms omitted for clarity. Gray, blue, purple, and green ellipsoids represent C, N, Cu, and F atoms, respectively.

Corresponding Cu–N distances differ by less than 0.03 Å between L^1 and L^2 copper complexes, and NCCN dihedral angles (≈ 5°) within a given chelate also show no significant differences. Significant differences are seen in the angles between like nitrogens of $Cu(L^1)_2$: N(py)–Cu–N(py) angle of 121.59(11)°, smaller, and N(pyrr)–Cu–N(pyrr) angle of 160.37(12), larger than in $Cu(L^2)_2$; $Cu(L^1)_2$ is thus the more "equatorial vacant TBP" of the two.

We also determined the structure of $Cu(L^0)_2$ crystallized from benzene (Figure 3). Comparison (Scheme 4) of the three $Cu(L^n)_2$ structures shows the following effects of progressive replacement of CF_3 by *t*Bu groups: the N(pyrr)–Cu–N(pyrr) angle increases (steps of 5° and 6°), the N(py)–Cu–N(py) angle decreases significantly (steps of 21° and 8°), but other angles change negligibly, and Cu–N distances become marginally (0.02 Å) shorter to pyrrolide.

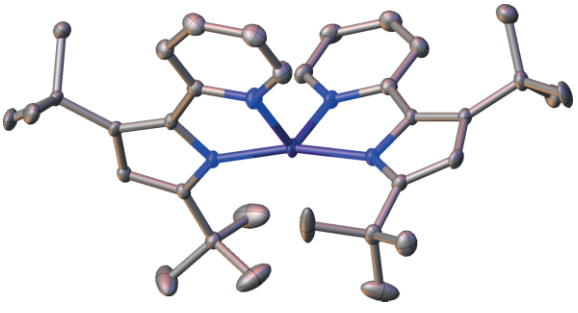

Figure 3. X-ray structure of $Cu(L^0)_2$, showing nitrogen atom labeling. Thermal ellipsoids shown at 50 % probability, hydrogen atoms omitted for clarity. Gray, blue, and purple ellipsoids represent C, N, and Cu atoms, respectively.

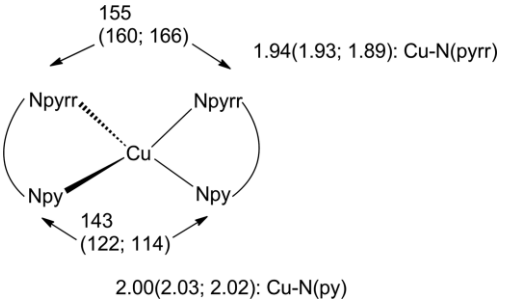

Scheme 4. Structural paramenters of $Cu(L^n)_2$: L^2(L^1; L^0) in Å, deg.

There are no significant differences in bond lengths within the pyridine or pyrrolide rings among these compounds. The overall change with increasing *t*Bu content is best described as progressive movement towards see-saw, (equatorially vacant TBP). These warrant comparison to the structure when there are no partially filled orbitals: $Zn(L^0)_2$. This structure is very close to tetrahedral (ZnNN interplanar angle 89°) with angle N(pyrr)–Zn–N(pyrr) 128° and angle N(py)–Zn–N(py) 119°. A structure of the zinc analog with *no* non-hydrogen substituents shows similar angles, 139° and 119°, so this distortion originates from electronic, not steric factors.[18] Thus, for constant ligand (L^0), there is a dramatic flattening from d^{10} to d^9 configuration, while the interplanar angle is similar, being nearly orthogonal.[4b]

A useful parameter to gauge the distortion of the coordination sphere from planarity in an $M(L^n)_2$ complex is the angle between the two planes defined by M and the two nitrogens of each chelate. For $Cu(L^n)_2$, the substituent dependence of this parameter, is especially large: 58°, 71°, and 82° for L^2, L^1, and L^0. These are probably best understood as avoiding *t*Bu group conflict with the pyridyl ring of the other chelate. Note that all of these angles are *more* than half way towards tetrahedral (90°), but none is truly tetrahedral, indicating some (electronic) resistance to the sterically preferred nearly tetrahedral structure, which is that adopted by $Zn(L^n)_2$.

NMR Characteristics

NMR spectra are presented (Figures S1 – S10) and discussed in detail in the Supporting Information. In general, the wide range in linewidths show that the extent of spin transmission is very different to the pyridyl vs. the pyrrolide rings.

DFT Geometries

DFT geometry optimization (see Supporting Information) of all three species $Cu(L^n)_2$ gave structures which were neither planar nor tetrahedral, and successfully capture (Table 1) many of the

Table 1. Geometric parameters [Å (°)] for the calculated and experimental $Cu(L^n)_2$ structures.

	Computed geometries			Experimental geometries		
	$[Cu(L^0)_2]$	$[Cu(L^1)_2]$	$[Cu(L^2)_2]$	$[Cu(L^0)_2]$	$[Cu(L^1)_2]$	$[Cu(L^2)_2]$
M–N(pyrr)	1.94	1.94	1.94	1.89	1.93	1.94
M–N(py)	2.09	2.10	2.10	2.02	2.03	2.00
N(pyrr)–M–N(pyrr)	162	163	165	166	160	155
N(py)–M–N(py)	112	113	129	114	122	143

experimentally observed features: the large angle between pyrrolide nitrogens and the small angle between the pyridyl nitrogens. In particular, the much smaller angle between pyridyl nitrogens for L^2 (vs. for the other L) is captured by DFT modeling.

The most significant structural trend is the N(py)–M–N(py) angle change of 20–30° (calculated and X-ray) for $L^0 \rightarrow L^2$; as we will see, this difference correlates with differences in the g_{xx}/g_{yy}-tensor values (vide infra) derived from EPR spectra.

EPR Spectroscopy

Complexes of Cu^{II} generally exhibit EPR spectra at room temperature and the series $Cu(L^{0,1,2})_2$ in toluene solution was no exception, however the spectra were not very informative. They are shown in Supporting Information (Figure S20).

The low temperature EPR spectra are more informative. Those recorded at X-band (≈ 9 GHz) at 77 K for the series $Cu(L^{0,1,2})_2$ are shown in Figure S21 (Supporting Information). Those for $Cu(L^{0,1})_2$ recorded at Q-band (35 GHz) at 2 K are shown in Figure 4. Spectra were also recorded for $Cu(L^2)_2$ at 224 GHz to achieve resolution of the small rhombic splitting (Figure S22, Supporting Information). Their combined analysis provided the parameters given in Table 2.

The EPR spectra of $Cu(L^2)_2$ are representative of tetragonally distorted Cu^{II}, whether distorted octahedral, square pyramidal or planar, as has been seen in many Cu^{II} complexes.[21] These are characterized by $g_{||} \approx 2.1–2.4$ and $g_{\perp} \approx 2.00–2.05$. Blumberg and Peisach[21a] have shown that a Cu^{II} complex with a *planar* dianionic N_4 equatorial donor set typically has $g_{||} \approx 2.2$ and $|A_{||}| \approx 600$ (±100) MHz. A well-known example is Cu(TPP) (TPP = 5,10,15,20-tetraphenylporphyrin dianion), and its precise parameters determined by a single crystal EPR/ENDOR study[19] are also given in Table 2. The $g_{||}$ and $|A_{||}|$ values for $Cu(L^2)_2$ are somewhat below the "normal" range, completely consistent with the reduction in symmetry vs. Cu(TPP), due to distinct donor nitrogens (pyridyl and pyrrolide) as well as their very different mutual angles, 155° and 143°. The situation for the other two complexes is quite different, consistent with their different CuN_4 angular parameters. In contrast to the nearly axial signal observed for $Cu(L^2)_2$,[22] the complexes of L^1 and L^0 exhibit nearly perfectly rhombic spectra. The rhombicity can be defined as $[(g_{max} - g_{mid})/(g_{max} - g_{min})]$, which is equal to 0 or 1 for a perfectly axial system and 0.5 for a perfectly rhombic system.

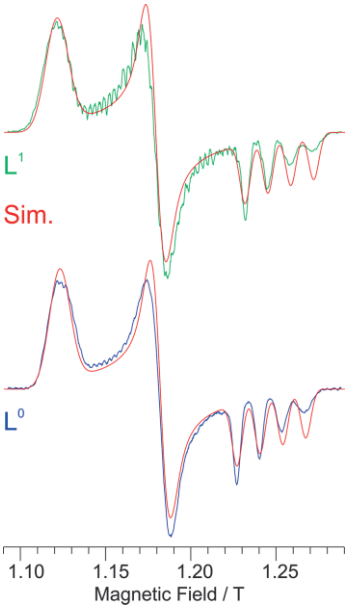

Figure 4. Q-band EPR spectra recorded at 2 K in frozen toluene solution (approx. 1 mM) for $Cu(L^n)_2$ $n = 0, 1$ respectively as blue and green traces, together with simulations (red traces). The ordinate scale is arbitrary. The spectra were recorded under passage conditions and appeared as absorption lineshapes; numerical first derivative spectra are shown for comparison with conventional EPR presentation. Experimental parameters: microwave frequency: 35.288 GHz (for $n = 0$), 35.433 GHz (for $n = 1$), 100 kHz field modulation amplitude, 1 G; time constant, 160 ms, scan time, 2 min. Simulation parameters are the same as at X-band (Table 2).

For $Cu(L^0)_2$, this parameter equals 0.507 and for $Cu(L^1)_2$, its value is 0.476. This sort of spectrum is typically observed for trigonal bipyramidal complexes, such as dimeric Cu(SalMe) [where SalMe is bis(*N*-methylsalicylaldiminate)],[20] and indeed the four nitrogens in $Cu(L^n)_2$ have angles which crudely resemble two axial (pyrrolides at about 163°) and two equatorial (pyridyls, at 118°) sites. For comparison, the EPR parameters for Cu(SalMe) are also shown in Table 2. This is not to imply that $Cu(L^0)_2$ and $Cu(L^1)_2$ are five-coordinate complexes, but that their geometry is very distorted from square planar, much more so than is $Cu(L^2)_2$.

DFT Calculation of EPR Parameters

The EPR parameters have been evaluated at the B3LYP/CP(TPP) level of theory[23] at the experimental geometry (Table 3). The

Table 2. EPR data for the series $Cu(L^{0,1,2})_2$, plus two comparison complexes. ^{63}Cu hyperfine coupling values in MHz.

Complex	g_{iso}, g_{avg}[a]	g_1 (max)	g_2 (mid)	g_3 (min)	A_{iso}[b]	A_1 (max)	A_2 (mid)	A_3 (min)
$Cu(L^0)_2$	2.13(1), 2.133	2.245(5)	2.132(2)	2.022(2)	140(20)	380(10)	–	–
$Cu(L^1)_2$	2.125(5) 2.142	2.258(2)	2.146(2)	2.023(2)	140(20)	380(10)	–	–
$Cu(L^2)_2$[c]	2.12(1) 2.118	2.238(2)	2.076(2)	2.041(2)	100(40)	450(10)	–	–
Cu(TPP)[d]	2.093	2.190	2.045	2.045	–273.5	–615	–102.7	–102.7
Cu(SalMe)[e]	2.13	2.25	2.13	2.02	243	393	195	141

[a] The value for g_{iso} was determined from the X-band spectra recorded at room temperature. The value for g_{avg} was determined from the 35 GHz spectra recorded at low temperature using: $g_{avg} = (g_1 + g_2 + g_3)/3$. [b] The value for A_{iso} (for ^{63}Cu, in MHz) was estimated from the X-band spectra recorded at room temperature except for Cu(TPP) and Cu(SalMe), where it is derived from the individual hyperfine components. No sign information is available here from EPR. Only the value for A_1 could be determined experimentally from the X- and Q-band spectra recorded at low temperature (77 K and 2 K, respectively). [c] The **g** matrix given here was derived from spectra recorded at 224 GHz (and 30 K); X-band spectra gave: $g_{||} = 2.240$, $g_{\perp} = 2.060$. [d] Data for single crystal Cu(TPP) in Zn(TPP)(H_2O) host taken from Brown and Hoffman.[19] [e] Data for single crystal Cu(SalMe) in Zn(SalMe) host taken from Bencini et al.[20]

g-tensor values calculated for the L^0 and L^1 species are quite similar, as observed experimentally. Absolute values of g_{zz} are relatively constant at ca. 2.22 for all the three species, consistent with experiment, while g_{xx} is larger by ≈ 0.02 and g_{yy} is smaller by ≈ 0.05 for L^2 (2.04 and 2.08) compared to the other two species (2.02 and 2.13). These differences originate in the geometries of the L^0 and L^1 species being quite similar, importantly the N(py)–M–N(py) angle, but distinctly different from L^2 in the X-ray structures. Consequently, more hybridization occurs (4 % in L^0 and L^1 compared to only 1 % in L^2, as tracked by Mulliken population analysis) with the 4s and the 4p orbital that lies parallel to the N(py)–N(py) line, due to the more see-saw and less square planar-like structure. Trends in the EPR *g* values thus reflect the experimental structural changes along the homologous series $Cu(L^n)_2$. Isotropic Fermi contact couplings (labeled *A*; sign of experimental values not determined) of –7, –107, and –254 MHz are calculated for the L^0, L^1, and L^2 species at their experimental geometries, respectively. While these values agree qualitatively with the experimental trend (the maximum hyperfine coupling component A_1 for L^2 is predicted to be larger than L^0 or L^1, as found), quantitative agreement is not strong, but is limited by the lack of experimental values for the A_2 and A_3 components. When there is a rigid geometry and a complete experimental dataset, as in [Cu(TPP)], the computational method gives good agreement between experiment and computed values for a small (four Ph replaced by four H) model Cu(porphyrin) (Table 3). Nevertheless, the trends in *A* values generally reflect the experimental bond angle changes, so EPR is a useful gauge of pyrrolide substituent influence on coordination sphere structure.

Table 3. Computed **g** and **A**(^{63}Cu) matrix values, the latter reported in MHz.

		g_{xx}	g_{yy}	g_{zz}	A_1	A_2	A_3	A_{avg}[b]
Cu(TPP)	DFT	2.063	2.063	2.193	–790	–81	–81	–317
	Exp.[a]	2.045	2.045	2.190	–615	–103	–103	–274
L^0	DFT@X-ray	2.016	2.129	2.207	–351	–48	379	–7
	Exp.	2.022	2.132	2.245	380	–	–	(140)
L^1	DFT@X-ray	2.026	2.131	2.225	–491	–100	270	–107
	Exp.	2.023	2.146	2.258	380	–	–	(140)
L^2	DFT@X-ray	2.052	2.083	2.216	–700	–90	29	–254
	Exp.	2.041	2.076	2.238	450	–	–	(100)

[a] Experimental sign information is available only for Cu(TPP), taken from Brown and Hoffman.[19] [b] Calculated using: $A_{avg} = (A_1 + A_2 + A_3)/3$; values in parentheses are estimates of A_{iso} from fluid solution spectra and are not directly comparable to values from the full hyperfine coupling matrix of solid samples.

Zn^{II} Complexes

These d^{10} complexes are valuable controls for both electronic and geometric structure of d^9 analogs. Synthesis of $Zn(L^2)_2$ occurs[4b] by addition of HL^2 to $ZnEt_2$ in 2:1 mol ratio in nonpolar solvent. Both reactants are mixed as colorless solutions (HL^2 in pentane and commercial $ZnEt_2$ in hexane) and within minutes at 25 °C a colorless precipitate forms; gas evolution is visible. After decanting, washing and drying, the ^{1}H and ^{19}F NMR of the white solid in C_6D_6 shows pure $Zn(L^2)_2$. The chemical shifts in the ^{1}H NMR have shifted from those of HL^2 and there is no sign of an acidic (NH) proton. Also, the ^{19}F NMR demonstrates that the two fluorine signals have shifted from the values found in HL^2. The NMR equivalence of the two ligands is consistent with C_2 symmetry. The colorless character indicates there is no energetically accessible metal-to-ligand charge transfer transition. The synthetic reaction from $ZnEt_2$ also proceeds well for the other two ligands, although it is slowest for the least acidic HL^0.

Given the structures for $Cu(L^n)_2$ described above, can $M(L^0)_2$ be tetrahedral? The calculated structures for M = Zn answer this in the affirmative as seen in Table 4. Here the difference in N(py)–Zn–N(py) (29–32°) is smaller than for M = Cu (36–50°). The distance Zn–N(pyrr) varies with substituent by 0.02 Å and Zn–N(py) varies by 0.04 Å.[24] These angular differences in particular provide further evidence that pyrrolide and pyridine are electronically very different ligands, hence produce a different ligand field from twofold symmetric ligands (e.g., 2,2′-bipyridyl).

Table 4. DFT optimized geometries [Å (°)] for $Zn(L^n)_2$ for the cases *n* = 2 and 0, showing structural influence of pyrrolide substituent.

Bond length, angle	L^2	L^0
Zn–N(py)	2.15	2.11
Zn–N(pyrr)	2.01	2.03
N(py)–Zn–N(py)	123.8	113.4
N(pyrr)–Zn–N(pyrr)	153.1	145.4

Mass Spectrometric Evidence for Oxidation

a. Copper

The CH_5^+ CI mass spectra of all three $Cu(L^n)_2$ complexes show signals for the parent monocation, indicating the existence of at least transient oxidized $[Cu(L^n)_2]^+$. For L^1 and L^2, fluoride loss is also an observed path to a cationic species, while for L^0 loss of CH_3 is favored, and observed, due to resonance stabilization of the resulting carbonium ion substituent. All three complexes also show protonation, via the [parent ion + 1] mass, due to basicity of the ligand; the amount of protonated complex ion falls off steeply from L^0 to L^1, and to L^2, in accord with ligand Brønsted basicity. The negative ion mass spectra show the intact monoanion for all three ligands, hence facile *reducibility*.

b. Zinc

We found that $Zn(L^2)_2$ shows a positive molecular ion by methane chemical ionization mass spectrometry, supporting that it is possible to oxidize the molecule, forming at least transient $[Zn(L^2)_2]^+$. Given the presence of electron withdrawing groups, we thought that $Zn(L^2)_2$ might also be prone to giving good negative ion mass spectra. Using slow electrons from chemical ionization (methane), we indeed see $[Zn(L^n)_2]^-$ as the predominant negative ion for both bis- and mono-CF_3 substituted ligand complexes. Most significantly, this means that it is possible to populate the π* orbital of these $Zn(L^n)_2$, so that redox noninnocence is established. Negative ion ESI MS for even the

most electron rich $Zn(L^0)_2$ shows an ion, but it is the methanol (solvent) adduct, $[Zn(L^0)_2(MeOH)]^-$. The mass spectrometric observation of $[Zn(L^n)_2]^+$ has significance beyond merely an analytical tool since it shows that loss of one electron from what might have been thought a redox inactive molecule can be accomplished. The molecule is thus electron rich, at least under these high energy (electron impact) ionization conditions.

DFT Calculation of Electronic Structure

Table 5 allows comparison of some structural parameters of $M(L^2)_2$ species from DFT geometry optimizations, all done to establish structural trends under the influence of changing number of d electrons. Among these divalent metals, both kinds of M/N distances increase by less than 0.09 Å from Ni to Zn. Angular parameters vary more dramatically, and show that zinc comes closest to "tetrahedral," and nickel has the largest inter-pyrrolide angle, but the smallest inter-pyridyl angle.[5d]

Table 5. Comparison of DFT geometry optimized structural parameters [Å (°)] of $M(L^2)_2$ for M = Ni, Cu, and Zn.

Bond length, angle	Ni[a]	Cu	Zn
M–N(py)	2.06	2.09	2.15
M–N(pyrr)	1.96	1.94	2.01
N(py)–M–N(py)	108.0	129.3	123.8
N (pyrr)–M–N(pyrr)	167.6	165.2	153.1

[a] Results for M = Ni are taken from Tsvetkov et al.[5d]

Comparison of the frontier orbitals of these species is enlightening. Figure 5 shows the frontier orbitals for $Cu(L^2)_2$, revealing that the upper four occupied orbitals (HOMO to HOMO-3) are all ligand-localized, namely pyrrolide π_{CC} in character with the two symmetry-equivalent pyrrolides contributing equally. Only the orbital at –7.688 eV (HOMO-4) shows some Cu 3d orbital character, and in a σ^*_{CuN} manner. This pattern of the frontier orbitals being localized at the ligand is found independent of the metal (see Supporting Information). Zinc has no significant d character among the range HOMO to HOMO-5. The LUMOs for all are pyridyl-localized, devoid of d metal character. For these late transition metals, the d orbitals are low enough in energy due to their large Z^* (effective nuclear charge) that the pyrrolide π orbitals are higher in energy.

For the Cu^{II} complexes, the unpaired spin density and the MO in which it is located (singly occupied MO, SOMO) can be calculated. Identification of the SOMO in an unrestricted calculation (i.e., Cu^{II}) requires an objective approach to identifying doubly occupied orbitals, which was done by calculation of

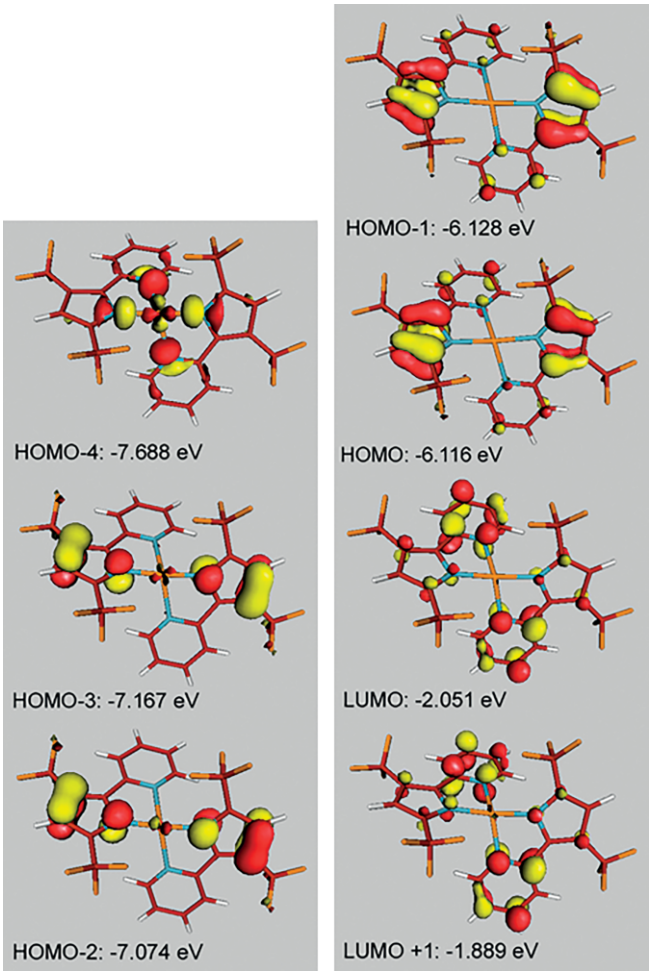

Figure 5. Isosurface drawings (iso = 0.05 au) of the alpha frontier orbitals of $Cu(L^2)_2$.

"corresponding orbitals".[25] Isosurface maps of the SOMO show no *major* spin differences among the three L^n complexes (Figure 6). The metal composition of the SOMO is mostly $d_{x^2-y^2}$, which is consistent with the EPR behavior, and it is σ-antibonding with respect to all four nitrogen lone pairs.

The spin densities are 60 % on copper with the remainder on the four nitrogens (each 10 %); see Figure S11 (Supporting Information). The spin density transmission into the ligand is evident from the range of proton NMR chemical shifts. Fluorine chemical shifts are also perturbed significantly from diamagnetic positions, but less so than the protons, due to the buffering effect of intervening sigma bonds. The detection (see be-

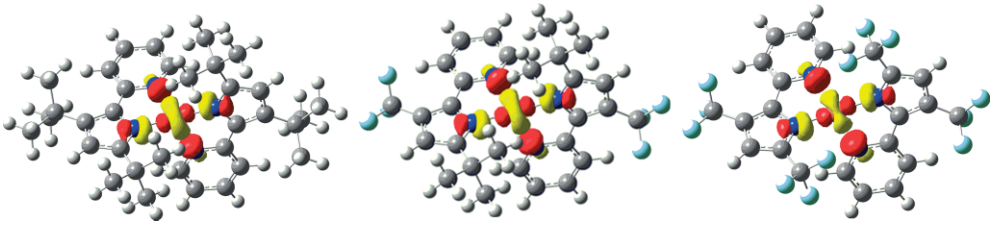

Figure 6. Isosurface maps of the singly occupied MO (SOMO) of $Cu(L^n)_2$ (iso = 0.05 au). Left, n = 0; middle, n = 1; right, n = 2.

low) of two oxidative events for these $M(L^n)_2$ is also supportive of ligand redox activity, since one cannot imagine *two* metal-centered oxidations of Cu^{II}. Adduct formation (e.g., DMAP and THF; see Supporting Information) by $Zn(L^2)_2$ shows that an inner sphere mechanism for oxidation is viable.

Oxidations of $M(L^n)_2$

a) Cyclic Voltammetric Behavior

These molecules have rich reversible electrochemistry, as observed by cyclic voltammetry (CV). As a preliminary consideration, we need to know the redox behavior of the ligand itself prior to evaluating that of its metal complexes. CV of the free acids HL^n is not relevant since the radical cation will have enhanced Brønsted acidity, and proton transfers will create rapid follow-up reactivity; for example, the excited states of HL are known[26] to have structures where the pyrrolide proton is located instead on the pyridine nitrogen, due to charge transfer at the excited state. In addition, oxidation of free pyrroles involves proton transfer as part of the cationic polymerization. CV of KL^n salts cannot be done since these were found to decompose the tetraalkylammonium cation in the supporting electrolyte.

We have therefore used the complexes $Zn(L^n)_2$ as the needed comparison standard, since these are undamaged by the electrochemical medium and mimic the electrochemistry of the anionic ligand attached to a redox inactive cation. We have used THF, CH_2Cl_2, MeCN, and 1,2-dichloroethane as solvents. For all three zinc complexes, there is no reductive chemistry (Pt button electrode, 0.1 M $[nBu_4N]PF_6$) down to the lowest potential employed (–1.5 V), but there is oxidation (Figure 7), consistent with redox chemistry derived from electron rich ligands. The trends in redox potential are consistent with expectation based on electron donating (*t*Bu) and electron withdrawing (CF_3) substituent character: CF_3 makes the observed oxidation potential more positive and *t*Bu makes oxidation less positive. $Zn(L^0)_2$ in CH_2Cl_2 shows two oxidation waves, both reversible at 25 mV/s in CH_2Cl_2; as CF_3 content increases, these waves move to higher potential, are less well separated from each other, and become irreversible. These $[Zn(L^n)_2]^+$ (n = 1, 2) cations are more reactive, hence less persistent, because their substituents make them more electrophilic. The behavior is similar, but less reversible in THF, suggesting solvent dependent follow-up reactivity of the cation.

For $Cu(L^n)_2$, the trends are similar on oxidation [two reversible oxidation waves for $Cu(L^0)_2$] in CH_2Cl_2 (Figure 7), but there is also a single reduction wave (Figure 8). Given the absence of this reduction for Zn^{II}, we attribute the reduction to mainly a $Cu^{II} \rightarrow Cu^{I}$ process. A DFT analysis of the geometric structures and frontier orbitals of these Cu^{I} species is given in Supporting Information. As CF_3 groups are introduced into the Cu complexes, the oxidation potentials become more positive, or disappear entirely and are certainly irreversible. The metal identity (Cu vs. Zn for the same L^n) does not significantly influence the potential values for these oxidations, consistent with *ligand localization* for the electron removed.

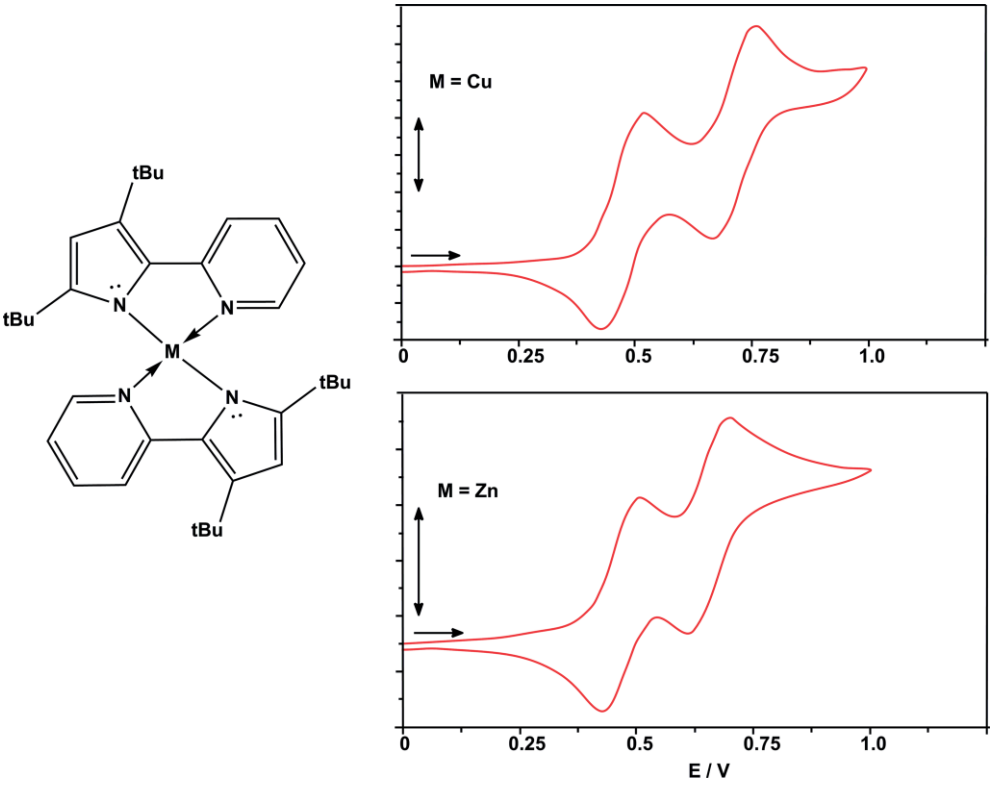

Figure 7. CV response of $Cu(L^0)_2$ (upper trace) and $Zn(L^0)_2$ (lower trace) with 0.1 M $TBAPF_6$ in CH_2Cl_2 at 25 mV s^{-1}. Vertical arrow shows 20 μA; Fc/Fc^+ = 0.0 V.

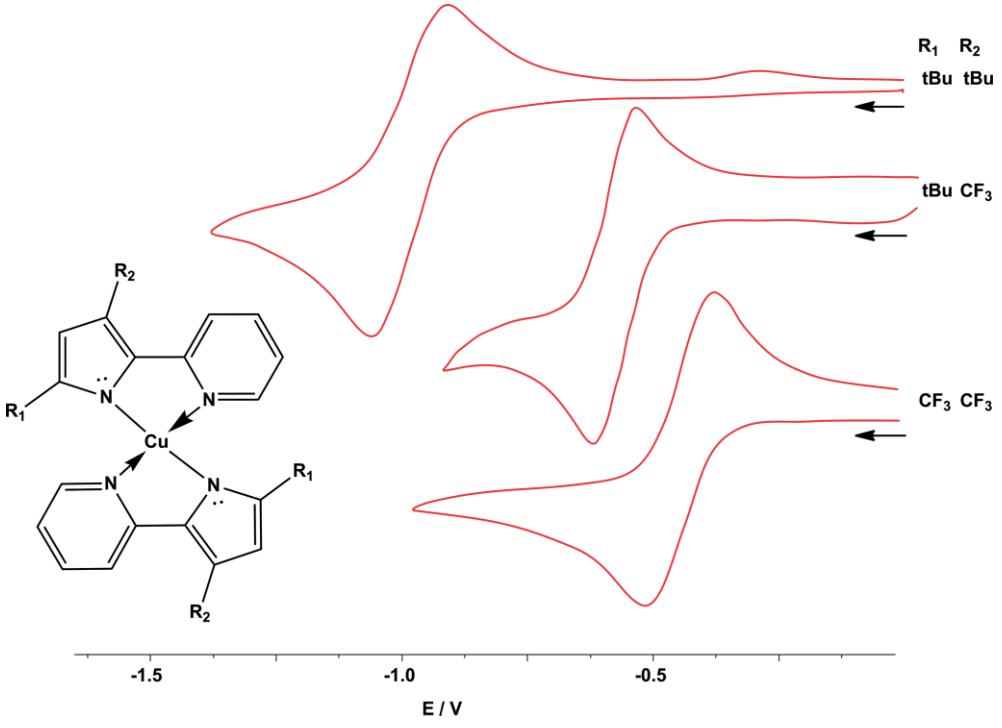

Figure 8. CV response of $Cu(L^n)_2$ with 0.1 M $TBAPF_6$ in THF at 25 mV s^{-1}.

DFT Evaluation of Oxidation Products

What are the geometric and electronic structures of these unusual species detected by mass spectrometry and by cyclic voltammetry: $[CuL_2]^+$, $[ZnL_2]^+$, and $[ZnL_2]^{2+}$? Zinc complexes, with their d^{10} configuration, are the comparison standard for learning the effect of partially filled d orbitals for copper or nickel. We have carried out DFT calculations, with geometry optimization, on certain oxidized species with the goal of finding out not only if the SOMO, after one electron removal, is essentially the HOMO of the unoxidized species, but also to evaluate when there *is* geometry change. One might have predicted, if oxidation occurs primarily at the ligand pyrrolide, that metal coordination geometry will be relatively unchanged.

Structural Correlations Among $[Zn(L^2)_2]^{q+}$ Species Where q = 0, 1, and 2

The calculated structural results on mono- (spin doublet) and dications (spin triplet) of $Zn(L^2)_2$ are shown in Table 6; our discussion will focus on comparison of the neutral to the doubly oxidized ion, to maximize impact of electron removal. Oxidation increases Zn–N(pyrr) distances by 0.04 Å, while the Zn–N(py) distances change by less than 0.012 Å. This indicates that oxidation is not uniformly felt, as it might if it occurred at the metal, but shows weakened binding ability focused on the pyrrolide.

This is the opposite of what is expected for oxidation at the metal center, which should create a stronger interaction with the formally anionic pyrrolide arm of the ligand. Distances within the pyridyl ring change negligibly (< 0.02 Å), while changes within pyrrolide are typically five times larger. Especially significant is that the oxidation lengthens pyrrolide Cα/Cβ, but shortens Cβ/Cβ. The origin of this is seen in the frontier MO diagrams of neutral $Zn(L^2)_2$ (Figure 9c, below), which shows that the HOMO of $Zn(L^n)_2$ is Cα/Cβ bonding, but Cβ/Cβ antibonding. Precisely the same trends are found for the analog $Zn(L^0)_2$ and its cations (see Supporting Information), showing that the effect is independent of pyrrolide substituent. These observations support the idea that the oxidation is correctly predicted by the frontier orbitals of ZnL_2 being ligand-localized; oxidation states of zinc higher than divalent are not involved. Oxidized *pyrrolide* is thus a weaker nucleophile for zinc, explaining the *longer* Zn–N(pyrr) distances in the cations; in contrast, Zn–N(py) distances shorten upon oxidation. The structural consequences of one electron oxidation of $Cu(L^2)_2$

Table 6. Comparison of bond lengths [Å] in $[Zn(L^2)_2]^{q+}$ with q = 0/1+/2+.

Bond	Neutral (S = 0)	Monocation (S = 1/2)	Dication (S = 1)
Zn–N1	2.007	2.023	2.045
Zn–N2	2.006	2.023	2.046
Zn–N3	2.153	2.144	2.146
Zn–N4	2.155	2.140	2.143
N1–C1	1.355	1.343	1.333
N1–C4	1.367	1.371	1.377
C1–C2	1.390	1.413	1.438
C2–C3	1.409	1.389	1.371
C3–C4	1.413	1.433	1.456
N3–C5	1.363	1.369	1.376
N3–C9	1.341	1.338	1.334
C5–C6	1.405	1.404	1.405
C6–C7	1.388	1.391	1.396
C7–C8	1.397	1.394	1.391
C8–C9	1.388	1.394	1.404

(see Supporting Information) likewise prove the electron is removed equally from the two pyrrolides.

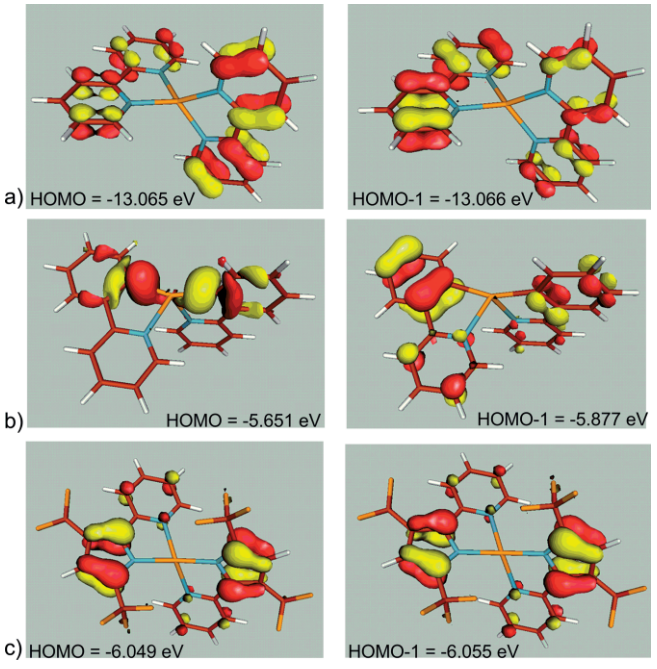

Figure 9. Isosurface diagrams (iso = 0.05 au) of frontier orbitals (HOMO, left column; HOMO-1, right column) of a) $[Zn(bpy)_2]^{2+}$, b) $Zn(phpy)_2$, and c) $Zn(L^2)_2$.

Electronic Effects of Chelate Asymmetry in a d^{10} Configuration

To what extent are angular distortions from tetrahedral structure due to the pyrrolide and pyridyl donors? Figure 9 shows the HOMO and HOMO-1 for the isoelectronic series $[Zn(bpy)_2]^{2+}$ (i.e., the complex with four identical imino N donors, 2,2′-bipyridyl), $Zn(phpy)_2$ [two imino and two carbanion donors, 2-(2-phenyl)pyridyl], and $Zn(L^2)_2$. The frontier orbitals are purely *ligand localized* for all three; d orbital participation is absent, showing how low the d orbital energy is for zinc. The dication with bpy (Figure 9a) has much lower orbital energies than the other two neutral complexes, due to its positive charge. The bpy case also has D_{2d} symmetry, with all inter-ligand N–Zn–N angles identical, but these orbitals are fully π_{CC} localized. The other two species show electronic differences between the two donors, with larger angles between the anionic donors and smaller angles between the pyridyls.

The phpy case (Figure 9b) has mainly π–phenyl character to the HOMO-1 and in the HOMO, it is Zn/C σ*. This has a "see-saw" geometry, with a large C–Zn–C angle. Note that the orbitals shown are essentially related by a C_2 axis, and thus the energies within each pair, differing primarily by phase, but not conjugated, are nearly degenerate. In summary, pyridyl and the anionic donor creates the "see-saw" structure because the pyrrolide and pyridyl ligands are electronically very different (anisotropic ligand field). The frontier orbitals for $Zn(L^2)_2$ show (Figure 9c) again illustrate pyrrolide to be the site of the most easily ionized electron.

Conclusions

The Cu and Zn bis-pyridylpyrrolides reported herein are electrochemically redox active, and the species thus formed have been shown by DFT calculations to have their oxidations focused at the pyrrolide rings. Thus, not only the geometric structures, but also the electronic structure of ions produced by mass spectrometry and by outer sphere electron transfer show the highly anisotropic character of bonding in pyridylpyrrolide complexes of the later 3d metals. In contrast, earlier in the 3d series (e.g., iron congeners), the d orbital energies rise among, then above those of pyrrolide, making their redox chemistry more conventionally metal-centered.

Experimentally, we offer CV and mass spectrometric evidence of these oxidation products, to complement the DFT work; isolation of such cations is clearly desirable. We have attempted this, but inevitably find HL^n as the major characterizable product on the laboratory timescale, and this observation shows that acidic conditions (e.g. $NAryl_3^+$) can lead to ready ligand loss from the oxidation product, as shown in other work.[6a]

The electronic effect of the pyrrolide CF_3 substituent is most dramatically demonstrated by the EPR spectra of $Cu(L^n)_2$, n = 0 1, 2. The observed g and $A(^{63}Cu)$ values indicate that the geometry changes from one with marked $d_{z^2}^1$ character, uncommon for four-coordinate Cu^{II}, for n = 0, 1, to typical square planar ($d_{x^2-y^2}^1$ ground state) for n = 2. Thus, the electron withdrawing substituents make the resulting Cu^{II} complex more "mundane". This experimental observation is corroborated by detailed quantum chemical computations of spin Hamiltonian parameters.

Thus the pyridylpyrrole ligand, as manifest in complexes of the most common ions that terminate the 3d series, namely Cu^{II} and Zn^{II}, has unique electronic, structural, and redox capabilities among its relatives making its complexes potentially useful for a variety of catalytic, including electrocatalytic, applications.

Experimental Section

General Procedures: All manipulations were carried out under an atmosphere of purified argon using standard Schlenk techniques or in a glovebox. Solvents were purchased from commercial sources, purified using Innovative Technology SPS-400 PureSolv solvent system or by distilling from conventional drying agents and degassed by the freeze-pump-thaw method twice prior to use. Glassware was oven-dried at 150 °C overnight. NMR spectra were recorded in C_6D_6, $[D_8]$THF and $[D_8]$toluene at 25 °C or 100 °C on a Varian Inova-400 spectrometer (^{1}H: 400.11 MHz, ^{19}F: 376.48 MHz). Proton chemical shifts are reported in ppm vs. Me_4Si, ^{19}F NMR chemical shifts are referenced relative to external CF_3CO_2H. X-band (≈ 9.2 GHz) EPR spectra were recorded on a modified Varian E-4 spectrometer at ambient temperature and at 77 K (using a liquid nitrogen finger Dewar). For Q-band (35 GHz) EPR measurements, a modified Varian E-109 spectrometer was used.[27] The Q-band spectrometer employs a Janis pumped liquid He immersion Dewar so that spectra are recorded at 2 K (superfluid He) under "passage" conditions which yield a dispersion signal which has an absorption lineshape;[28] digital first derivative spectra are also shown for easier comparison with conventional EPR spectral presentation. High field/frequency EPR

(HFEPR) spectra were also recorded at the EMR Facility of the National High Magnetic Field Laboratory, Tallahassee, FL using a spectrometer described elsewhere.[29] EPR simulations employed the program QPOW, by R. L. Belford,[30] as modified by J. Telser.

Mass spectrometry analyses were performed in an Agilent 6130 MSD (Agilent Technologies, Santa Clara, CA) quadrupole mass spectrometer equipped with a Multimode (ESI and APCI) source. High resolution mass spectra were obtained on a ThermoFinnigan MAT95XP mass spectrometer. Electrochemical studies were carried out with an Autolab model PGSTAT30 potentiostat (Eco Chemie). A three-electrode configuration consisting of a working electrode (platinum button electrode), and $Ag/AgNO_3$ (0.01 M in MeCN with 0.1 M nBu_4NPF_6) reference electrode, and a platinum coil counter electrode was used. All electrochemical potentials were referenced with respect to the Cp_2Fe/Cp_2Fe^+ redox couple, added internally with the sample. Magnetic susceptibilities were measured in a concentric NMR tube, using hexamethylbenzene as internal standard. Electronic absorption spectra were measured on a Varian Cary 5000 UV/Vis-NIR spectrometer. Diethylzinc in hexanes (15 % by weight), 4-dimethylaminopyridine (DMAP), copper(I) triflate, potassium hydride and thallium ethoxide were purchased from commercial sources. HL^0, HL^1 were synthesized following published procedures.[4a,6d] Our structure determination of $Cu(L^1)_2$ here shows that the previously reported *location* of the CF_3 substituent in molecule HL^1 is incorrect; it is located near the pyridyl, not adjacent to the pyrrole nitrogen. We confirmed that we have synthesized the same HL^1 as obtained earlier, by identity of the NMR chemical shifts. We have also reported the crystal structure of HL^1 itself,[31] showing this same, corrected connectivity (Scheme 5).

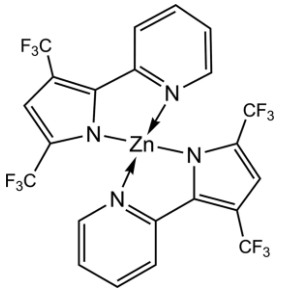

Scheme 5.

$Zn(L^2)_2$: 100.0 mg (0.357 mmol) of HL^2 was dissolved in 12 mL of pentane yielding a clear solution. To this solution, 146.9 mg (0.178 mmol) of $ZnEt_2$ in hexanes (15 % by weight) was added. In time of mixing, gas evolution was observed; white precipitate then formed while the solution remained colorless. After 15 minutes, solvent was pumped off and resulting white solid was collected. Full conversion of the starting material to the single product, ZnL^2_2 was observed. Yield, to a single product, is quantitative by fluorine and proton NMR spectroscopy. Mp: 143 °C–144 °C. ^1H NMR (25 °C, C_6D_6): δ = 7.92 (d, *J* = 8.4 Hz, 1 H), 7.09 (s, 1 H), 6.75–6.79 (m, 2 H), 6.05 (t, *J* = 7.2 Hz, 1 H). ^{19}F NMR (25 °C, C_6D_6): δ = –61.2, –55.2 (s). MS (CI, negative): Found, 621.9994. $C_{22}H_{10}F_{12}N_4Zn$ Calc. 622.0005. MS (EI, positive): 622.0007 (Scheme 6).

$Zn(L^1)_2$: 100.0 mg (0.373 mmol) of HL^1 was dissolved in 12 mL of pentane yielding a clear solution. To this solution, 153.5 mg (0.186 mmol) of $ZnEt_2$ in hexanes (15 % by weight) was added. In time of mixing, the solution turned a light yellow color. The solvent was pumped off and the resulting off-white solid was collected. Conversion of the starting material to the single product, ZnL^1_2 was complete within 15 min. Yield: 98 % by fluorine NMR spectroscopy.

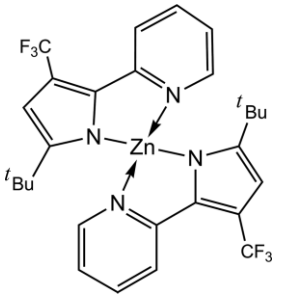

Scheme 6.

Mp: 168 °C–170 °C. ^1H NMR (25 °C, C_6D_6): δ = 1.13 (s, 9 H), 6.02 (m, *J* = 5.6 Hz, 1 H), 6.85 [td, *J* = 7.2 Hz (t), *J* = 1.6 Hz(d), 1 H], 6.85 (s, 1 H), 6.91 (d, *J* = 4.8 Hz, 1 H), 8.06 (d, *J* = 8.8 Hz, 1 H). ^{19}F NMR (25 °C, C_6D_6): δ = –54.3 (s). MS (CI, negative): Found, 598.1504. $C_{28}H_{28}F_6N_4Zn$ Calc. 598.1510. MS (EI, positive): 598.1490 (Scheme 7).

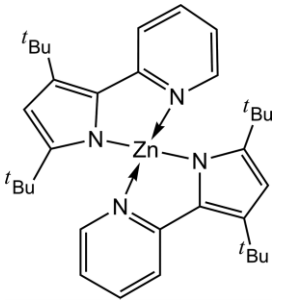

Scheme 7.

$Zn(L^0)_2$: 100.0 mg (0.390 mmol) of HL^0 was dissolved in 12 mL of pentane yielding a clear solution. To this solution, 160.6 mg (0.195 mmol) of $ZnEt_2$ in hexanes (15 % by weight) was added. In time of mixing, the solution turned a light green color. The solvent was pumped off and the resulting yellow solid was collected, and only about 30 % conversion of starting material to product is observed after 15 min by ^1H NMR spectroscopy. Full conversion of the starting material to the single product, ZnL^0_2 was observed only after 2 hours. Yield: 97 % by proton NMR spectroscopy. Mp: 179 °C–181 °C. ^1H NMR (25 °C, C_6D_6): δ = 1.34 (s, 9 H), 1.628 (s, 9 H), 5.99 (t, *J* = 6.4 Hz, 1 H), 6.59(s, 1 H), 6.93[td, *J* = 7.6 Hz (t), 1.6 Hz (d), 1 H], 7.27(d, *J* = 4.8 Hz, 1 H), 7.89(d, *J* = 8.4 Hz, 1 H). These data compare satisfactorily to those reported.[4b]

$Cu(L^0)_2$: To a Et_2O solution (10 mL) of HL^0 (0.15 g, 0.59 mmol) KH (0.026 g, 0.64 mmol, 10 % excess) was added at room temperature whilst stirring. The mixture turned to yellow color over a few minutes and was left to react for 30 min; gas evolution was observed over this period of time. Following 5 min for settling, this was filtered through Celite. $Cu(OTf)_2$ (0.107 g, 0.30 mmol) was added and the solution stirred for 6 more hours. The resulting mixture was filtered through Celite to remove KOTf, to yield a dark yellow solution. After evaporation of the solvent a dark brown solid was obtained. Dark yellow-greenish crystals were grown by slow evaporation of ether at room temperature. Yield: 0.143 g (86 %). Mp: 236–240 °C. ^1H NMR([D_8]toluene, 100 °C): δ = 38.3 (br., $\nu_{1/2}$ = 7.89 KHz, *H*-aromatic), 9.6 (br., $\nu_{1/2}$ = 114 Hz, *H*-aromatic), 8.9 (br., $\nu_{1/2}$ = 386 Hz, 5-*t*Bu), 2.40 (br., $\nu_{1/2}$ = 33 Hz, 3-*t*Bu). Spectra at temperatures higher than room temp. are generally sharper, and (the temperature dependent) chemical shifts also move towards the diamagnetic region for each specific functionality. HR-MS(CI, positive): Exp: 573.30

$[^{63}CuL^0{}_2]^+$, $C_{34}H_{46}N_4{}^{63}Cu$, Calc: 573.30; Exp: 574.31 $[^{63}CuL^0{}_2 + H]^+$, Calc: 574.31; Exp: 558.28 $[^{63}CuL^0{}_2\text{-}CH_3]^+$, Calc: 558.27. HR-MS(CI, negative): Exp: 573.30 $[^{63}CuL^0{}_2]^-$, Calc: 5 73.30; also seen is the ^{13}C isotopomer. For each ion here and below, the ^{65}Cu isotopomers were also seen in the correct abundance. Magnetic susceptibility: X_g (10^{-6}) = 2.20. μ_{eff} (BM) = 1.81. UV/Vis in C_6D_6, λ_{max}(nm) = 340, 394, 650, 795. Crystals for X-ray structure determination were grown from Et_2O. The deprotonation of HL^1 is problematic if product is left in contact with KH for longer periods, giving green solutions; this is the reason for the changed deprotonating agent for HL^1 below.

$Cu(L^1)_2$: To an ethereal solution, 10 mL, of HL^1 (0.213 g, 0.79 mmol), thallium ethoxide (0.198 g, 0.79 mmol) dissolved in ether, 5 mL, was added dropwise at room temperature and the solution left to stir for 4 hours; the solution color turned yellow immediately. Then, $Cu(OTf)_2$ (0.124 g, 0.34 mmol) was added while the mixture developed a green color over few minutes. It was left to react overnight and then left to settle for 5 min. It was filtered through Celite to yield a dark green solution after removal of TlOTf. The filtrate was pumped dry to obtain a green powder. Dark green crystals of the title compound were grown by slow evaporation from pentane/benzene (3:1) solution at room temperature. Yield: 0.042 g (24 %). Mp: 145 °C (change color), 177–180 °C (dec). ^{19}F NMR([D_8]toluene, 25 °C): δ = = –39.9 (br., $\nu_{1/2}$ = 1.62 kHz, 3-CF_3). ^{19}F NMR([D_8]toluene, 100 °C): δ = –41.9 (br., $\nu_{1/2}$ = 0.79 kHz, 3-CF_3). ^1H NMR([D_8]toluene, 100 °C): δ = 36.1 (br., $\nu_{1/2}$ = 5.35 kHz, *H*-aromatic), 10.2 (br., $\nu_{1/2}$ = 112 Hz, *H*-aromatic), 9.3 (br., $\nu_{1/2}$ = 446 Hz, 3-*t*Bu). HR-MS(CI, positive): Exp: 597.15 $[^{63}CuL^1{}_2]^+$, $C_{28}H_{28}N_4F_6{}^{63}Cu$, Calc: 597.15; Exp: 598.15 $[^{63}CuL^1{}_2 + H]^+$, Calc: 598.15; Exp. 578.15 $[^{63}CuL^1{}_2\text{-}F]^+$, Calc: 578.15. HR-MS(CI, negative): Exp: 597.15 $[^{63}CuL^1{}_2]^-$, Calc: 597.15. Magnetic susceptibility: X_g (10^{-6}) = 2.80. μ_{eff} (BM) = 2.01. UV/Vis in C_6D_6, λ_{max}(nm) = 317, 373, 663, 810. Crystals for X-ray structure determination were grown from pentane:benzene (3:1).

$Cu(L^2)_2$: HL^2 (0.15 g, 0.54 mmol) was dissolved in diethyl ether (10 mL) and KH (0.024 g, 0.59 mmol) added at room temperature. A white dispersion is formed with release of abundant bubbles, which ended within 3 min. The dispersion was left to stir for 15 min and $Cu(OTf)_2$ (0.097 g, 0.27 mmol) was added whilst stirring. The mixture turned to grey color almost immediately and then to blue. After 5 min the deep blue and homogeneous solution was filtered through Celite; longer time here results in color change to yellow brown, which was not further investigated. The filtrate was pumped dry to yield a blue solid of the title compound. It can be recrystallized from benzene by slow evaporation. Yield: 0.148 g (89 %). Mp: 122–124 °C. ^{19}F NMR([D_8]toluene, 25 °C): δ = –44.6 (br., $\nu_{1/2}$ = 1.17 kHz, 3-CF_3), –73.5 (br., $\nu_{1/2}$ = 2.29 kHz, 5-CF_3). ^{19}F NMR([D_8]toluene, 100 °C): δ = –46.4 (br., $\nu_{1/2}$ = 0.72 kHz, 3-CF_3), –67.9 (br., $\nu_{1/2}$ = 0.89 kHz, 5-CF_3). ^1H NMR([D_8]toluene, 100 °C): δ = 37.9 (br., $\nu_{1/2}$ = 6.39 kHz, *H*-aromatic), 9.65 (br., $\nu_{1/2}$ = 94 Hz, *H*-aromatic). HR-MS(CI, positive): Exp: 621.00 $[^{63}CuL^2{}_2]^+$, $C_{22}H_{10}N_4F_{12}{}^{63}Cu$, Calc: 621.00. HR-MS(CI, negative): Exp: 621.00 $[^{63}CuL^2{}_2]^-$, Calc: 621.00. Both positive and negative ion spectra also show loss of one F. Magnetic susceptibility: X_g (10^6) = 3.26. μ_{eff} (BM) = 2.12. UV/Vis in C_6D_6, λ_{max}(nm) = 271, 341, 601, 705. Crystals for X-ray structure determination were grown by slow evaporation from benzene.

Supporting Information (see footnote on the first page of this article): Full details on crystallographic work and DFT calculations, together with NMR and EPR/HFEPR spectra are available. Crystallographic data (excluding structure factors) for the structures in this paper have been deposited with the Cambridge Crystallographic Data Centre,

CCDC 1874688 (for **$Cu(L^2)_2$**), 1874689 (for **$Cu(L^1)_2$**), and 1874690 (for **$Cu(L^0)_2$**) contain the supplementary crystallographic data for this paper. These data can be obtained free of charge from The Cambridge Crystallographic Data Centre.

Acknowledgments

This work was supported by the U.S. National Science Foundation (NSF). The structural work at NSF's ChemMatCARS Sector 15 is principally supported by the (NSF) Divisions of Chemistry (CHE) and Materials Research (DMR), under grant number CHE-1346572. Use of the Advanced Photon Source, an Office of Science User Facility operated for the U.S. Department of Energy (DOE) Office of Science by Argonne National Laboratory, was supported by the DOE under Contract No. DE-AC02-06CH11357. We thank Prof. Brian M. Hoffman, Northwestern University, for use of the 35 GHz EPR spectrometer, which is supported by NSF grant number MCB-1118613. We thank Dr. Andrew Ozarowski for the HFEPR measurement at the NHMFL, which is funded by NSF through Cooperative Agreements DMR-0654118 and DMR-1644779, and the State of Florida. RLL thanks Prof. H. Bernhard Schlegel, Wayne State University, for helpful discussions and financial support through DOE grant DE-FG02-09ER16120 and Grand Valley State University Start-Up funds. The Wayne State Grid is acknowledged for computational resources. Dr. Xinfeng Gao is thanked for insights into NMR of paramagnetic compounds.

Keywords: Coordination chemistry · Pyrroles · EPR · Density functional calculations

[1] a) P. J. Derrick, L. Åsbrink, O. Edqvist, B. Ö. Jonsson, E. Lindholm, *Int. J. Mass Spectrom. Ion Phys.* **1971**, *6*, 191–202; b) P. J. Derrick, L. Åsbrink, O. Edqvist, E. Lindholm, *Spectrochim. Acta Part A* **1971**, *27*, 2525–2537.

[2] a) C. Hansch, H. Gao, *Chem. Rev.* **1997**, *97*, 2995–3060; b) C. Jones, R. P. Rose, *New J. Chem.* **2007**, *31*, 1484–1487; c) R. A. Jones, T. M. Spotswood, P. Cheuychit, *Tetrahedron* **1967**, *23*, 4469–4479.

[3] a) E. Campazzi, E. Solari, R. Scopelliti, C. Floriani, *Inorg. Chem.* **1999**, *38*, 6240–6245; b) R. Crescenzi, E. Solari, C. Floriani, A. Chiesi-Villa, C. Rizzoli, *Inorg. Chem.* **1998**, *37*, 6044–6051; c) J. J. H. Edema, S. Gambarotta, A. Meetsma, F. Van Bolhuis, A. L. Spek, W. J. J. Smeets, *Inorg. Chem.* **1990**, *29*, 2147–2153; d) J. Hao, H. Song, C. Cui, *Organometallics* **2009**, *28*, 3100–3104; e) S. Ilango, B. Vidjayacoumar, S. Gambarotta, S. I. Gorelsky, *Inorg. Chem.* **2008**, *47*, 3265–3273; f) A. J. Jiang, J. H. Simpson, P. Müller, R. R. Schrock, *J. Am. Chem. Soc.* **2009**, *131*, 7770–7780; g) E. R. King, T. A. Betley, *J. Am. Chem. Soc.* **2009**, *131*, 14374–14380; h) I. Korobkov, S. Gambarotta, *Organometallics* **2009**, *28*, 5560–5567; i) I. Korobkov, S. Gambarotta, G. P. A. Yap, *Organometallics* **2001**, *20*, 2552–2559; j) J. B. Love, *Chem. Commun.* **2009**, 3154–3165; k) A. Novak, A. J. Blake, C. Wilson, J. B. Love, *Chem. Commun.* **2002**, 2796–2797; l) I. Saeed, S. Katao, K. Nomura, *Organometallics* **2009**, *28*, 111–122; m) G. T. Sazama, T. A. Betley, *Inorg. Chem.* **2010**, *49*, 2512–2524; n) E. Solari, R. Crescenzi, D. Jacoby, C. Floriani, A. Chiesi-Villa, C. Rizzoli, *Organometallics* **1996**, *15*, 2685–2687; o) A. Spannenberg, V. Burlakov Vladimir, P. Arndt, M. Klahn, U. Rosenthal, *Z. Kristallogr. New Cryst. Struct.* **2007**, *222*, 192; p) K. Yünlü, F. Basolo, A. L. Rheingold, *J. Organomet. Chem.* **1987**, *330*, 221–236.

[4] a) J. J. Klappa, A. E. Rich, K. McNeill, *Org. Lett.* **2002**, *4*, 435–437; b) J. J. Klappa, S. A. Geers, S. J. Schmidtke, L. A. MacManus-Spencer, K. McNeill, *Dalton Trans.* **2004**, 883–891.

[5] a) J. A. Flores, J. G. Andino, N. P. Tsvetkov, M. Pink, R. J. Wolfe, A. R. Head, D. L. Lichtenberger, J. Massa, K. G. Caulton, *Inorg. Chem.* **2011**, *50*, 8121–8131; b) K. Searles, M. Pink, K. G. Caulton, D. J. Mindiola, *Dalton Trans.* **2012**, *41*, 9619–9622; c) K. Searles, A. K. Das, R. W. Buell, M. Pink, C.-H. Chen, K. Pal, D. G. Morgan, D. J. Mindiola, K. G. Caulton, *Inorg. Chem.* **2013**, *52*, 5611–5619; d) N. P. Tsvetkov, C.-H. Chen, J. G. Andino, R. L.

Lord, M. Pink, R. W. Buell, K. G. Caulton, *Inorg. Chem.* **2013**, *52*, 9511–9521.

[6] a) J.-L. Chen, C.-H. Lin, J.-H. Chen, Y. Chi, Y.-C. Chiu, P.-T. Chou, C.-H. Lai, G.-H. Lee, A. J. Carty, *Inorg. Chem.* **2008**, *47*, 5154–5161; b) A. T. Luedtke, K. I. Goldberg, *Inorg. Chem.* **2007**, *46*, 8496–8498; c) J. L. McBee, T. D. Tilley, *Organometallics* **2009**, *28*, 3947–3952; d) D. Pucci, I. Aiello, A. Aprea, A. Bellusci, A. Crispini, M. Ghedini, *Chem. Commun.* **2009**, 1550–1552; e) S. Schouteeten, O. R. Allen, A. D. Haley, G. L. Ong, G. D. Jones, D. A. Vicic, *J. Organomet. Chem.* **2006**, *691*, 4975–4981; f) P.-I. Shih, C.-H. Chien, C.-Y. Chuang, C.-F. Shu, C.-H. Yang, J.-H. Chen, Y. Chi, *J. Mater. Chem.* **2007**, *17*, 1692–1698.

[7] a) C. P. Andrieux, P. Hapiot, P. Audebert, L. Guyard, M. N. Dinh An, L. Groenendaal, E. W. Meijer, *Chem. Mater.* **1997**, *9*, 723–729; b) P. Audebert, L. Guyard, M. N. Dinh An, P. Hapiot, M. Chahma, C. Combelas, A. Thiebault, *J. Electroanal. Chem.* **1996**, *407*, 169–173; c) L. Guyard, P. Hapiot, P. Neta, *J. Phys. Chem. B* **1997**, *101*, 5698–5706; d) D. E. Raymond, D. J. Harrison, *J. Electroanal. Chem.* **1993**, *361*, 65–76; e) S. Petruso, S. Caronna, S. Gambino, G. Filardo, G. Silvestri, *J. Heterocycl. Chem.* **1991**, *28*, 793–796.

[8] Substitution at the pyridine ring is also possible, and a four-coordinate Zn^{II} complex with pyridine pyrrolide coordination from the anion of 6-(1*H*-pyrrol-2-yl)-2-(2,6-diisopropylphenyl)iminopyridine has been reported,[9] but the imino substituent is potentially an additional ligand and thus does not fit into the present study.

[9] I. D'Auria, C. Tedesco, M. Mazzeo, C. Pellecchia, *Dalton Trans.* **2017**, *46*, 12217–12225.

[10] H. Xu, J. B. Diccianni, J. Katigbak, C. Hu, Y. Zhang, T. Diao, *J. Am. Chem. Soc.* **2016**, *138*, 4779–4786.

[11] T. F. Mastropietro, A. Aprea, M. La Deda, I. Aiello, M. Ghedini, A. Crispini, *Cryst. Growth Des.* **2012**, *12*, 2173-2177.

[12] a) J. L. McBee, T. D. Tilley, *Organometallics* **2010**, *29*, 184–192; b) M. L. Clement, K. A. Grice, A. T. Luedtke, W. Kaminsky, K. I. Goldberg, *Chem. Eur. J.* **2014**, *20*, 17287–17291.

[13] Y.-P. Wang, X.-H. Hu, Y.-F. Wang, J. Pan, X.-Y. Yi, *Polyhedron* **2015**, *102*, 782–787.

[14] A. Szentkuti, J. A. Garg, O. Blacque, K. Venkatesan, *Inorg. Chem.* **2015**, *54*, 10748–10760.

[15] a) N. Komine, R. W. Buell, C.-H. Chen, A. K. Hui, M. Pink, K. G. Caulton, *Inorg. Chem.* **2014**, *53*, 1361–1369; b) K. Searles, S. Fortier, M. M. Khusniyarov, P. J. Carroll, J. Sutter, K. Meyer, D. J. Mindiola, K. G. Caulton, *Angew. Chem. Int. Ed.* **2014**, *53*, 14139–14143; *Angew. Chem.* **2014**, *126*, 14363–14367; c) L. N. Grant, M. E. Carroll, P. J. Carroll, D. J. Mindiola, *Inorg. Chem.* **2016**, *55*, 7997–8002.

[16] a) G. H. Imler, Z. Lu, K. A. Kistler, P. J. Carroll, B. B. Wayland, M. J. Zdilla, *Inorg. Chem.* **2012**, *51*, 10122–10128; b) A. McSkimming, V. Diachenko, R. London, K. Olrich, C. J. Onie, M. M. Bhadbhade, M. P. Bucknall, R. W. Read, S. B. Colbran, *Chem. Eur. J.* **2014**, *20*, 11445–11456.

[17] J. L. Franklin, *J. Am. Chem. Soc.* **1950**, *72*, 4278–4280.

[18] H. Wang, Y. Zeng, J. S. Ma, H. Fu, J. Yao, A. I. Mikhaleva, B. A. Trofimov, *Chem. Commun.* **2009**, 5457–5459.

[19] T. G. Brown, B. M. Hoffman, *Mol. Phys.* **1980**, *39*, 1073–1109.

[20] A. Bencini, I. Bertini, D. Gatteschi, A. Scozzafava, *Inorg. Chem.* **1978**, *17*, 3194–3197.

[21] a) W. E. Blumberg, J. Peisach, *Arch. Biochem. Biophys.* **1974**, *165*, 691–708; b) B. J. Hathaway, D. E. Billing, *Coord. Chem. Rev.* **1970**, *5*, 143–207.

[22] Use of very high frequency EPR, at 224 GHz, allowed resolution of slight rhombic splitting in $Cu(L^2)_2$: g_{mid} = 2.076, g_{min} = 2.041, which values average to $g_{\perp}$ = 2.06; in contrast to Cu(TPP), $Cu(L^2)_2$ would not be expected to give perfectly axial symmetry due to the lack of a fourfold symmetry axis.

[23] F. Neese, *Inorg. Chim. Acta* **2002**, *337*, 181–192.

[24] The effects of steric bulk of the *t*Bu are seen by comparison to the structure of another ZnL_2 with methyls located where $Zn(L^0)_2$ has *t*Bu groups.[4b] The methyl analog shows angle N(pyrr)-Zn-N(pyrr) of 135° (larger than for *t*Bu) and angle N(py)-Zn-N(py) 105° (smaller). Both represent movement which has nothing obvious to do with steric bulk of ^{t}Bu, but seem to involve pyrrolide donors becoming more *transoid*.

[25] a) A. T. Amos, G. G. Hall, *Proc. R. Soc. London Ser. A Proc. R. Soc. London Ser. B Proc. Roy. Soc. A* **1961**, *263*, 483–493; b) P. O. Löwdin, *J. Appl. Phys.* **1962**, *33*, 251–280; c) R. L. Martin, E. R. Davidson, *Phys. Rev. A* **1977**, *16*, 1341–1346; d) F. Neese, *J. Phys. Chem. Solids* **2004**, *65*, 781–785.

[26] P. J. Morgan, A. J. Fleisher, V. Vaquero-Vara, D. W. Pratt, R. P. Thummel, M. Kijak, J. Waluk, *J. Phys. Chem. Lett.* **2011**, *2*, 2114–2117.

[27] M. M. Werst, C. E. Davoust, B. M. Hoffman, *J. Am. Chem. Soc.* **1991**, *113*, 1533–1538.

[28] C. Mailer, C. P. S. Taylor, *Biochim. Biophys. Acta* **1973**, *322*, 195–203.

[29] A. K. Hassan, L. A. Pardi, J. Krzystek, A. Sienkiewicz, P. Goy, M. Rohrer, L.-C. Brunel, *J. Magn. Reson.* **2000**, *142*, 300–312.

[30] a) R. L. Belford, G. G. Belford, *J. Chem. Phys.* **1973**, *59*, 853–854; b) R. L. Belford, M. J. Nilges, in *EPR Symposium, 21st Rocky Mountain Conference*, Denver, Colorado, **1979**.

[31] J. G. Andino, J. A. Flores, J. A. Karty, J. P. Massa, H. Park, N. P. Tsvetkov, R. J. Wolfe, K. G. Caulton, *Inorg. Chem.* **2010**, *49*, 7626–7628.

Received: August 1, 2018

